EurJIC
European Journal of Inorganic Chemistry

Research Article
doi.org/10.1002/ejic.202300282

Chemistry Europe
European Chemical Societies Publishing

www.eurjic.org

One and Two-Dimensional 1,4-Xylylenediammonium (pXDA) Lead Halides: Powders and Thin Films

Gonzalo García-Espejo,[a] Konstantis F. Konidaris,*[a] Pietro Anzini,[a] Stefano Brenna,[a] Antonietta Guagliardi,[b] and Norberto Masciocchi*[a]

The discovery of new 3D perovskites and their 2D and 1D analogues continues to attract the interest of the scientific community and therefore the understanding of their structural, optical, and physicochemical properties is of fundamental importance. Here, we report the one-pot synthesis and the full characterization of 1D and 2D lead halide polycrystalline solids containing the rather rigid 1,4-xylylenediammonium (pXDA) organic cation as spacer. We isolated 2D Dion-Jacobson (DJ) perovskites, namely (pXDA)PbX_4 (X=Cl, Br) and the mixed halide (pXDA)$Pb(Br_{1-x}I_x)_4$ species (all based on 2D monolayers of corner-sharing lead halide octahedra), and, for iodine, the (pXDA)$Pb_2I_6 . 2H_2O$ phase, which contains 1D $\left[PbI_3^-\right]_\infty$ ribbons. The latter species can be reversibly dehydrated by gentle heating, forming the isomorphous (pXDA)Pb_2I_6. crystal phase. These species, some of which have recently been studied in the frame of broad light emitters and for photovoltaic applications, have been characterized by variable-temperature X-ray diffraction methods, shedding light onto their anisotropic thermal responses, of utmost importance for day-night cycling in functional devices. Spin-coated thin films were also prepared and studied by means of synchrotron radiation grazing incidence X-ray diffraction, SEM imaging and fluorescence spectroscopy experiments.

Introduction

During the last decade, the scientific community has witnessed the skyrocketing of hybrid organic-inorganic halide perovskites as semiconducting materials that revolutionized the field, mostly thanks to their excellent optoelectronic properties, low exciton binding energy, long carrier diffusion length and easy fabrication methods.[1–7] Indeed, the latter outstanding features make them suitable alternatives for a broad range of applications: photovoltaic devices,[8,9] light-emitting diodes (LEDs),[10,11] detectors,[12,13] sensors[14] and lasing.[15]

Among the different families of hybrid organic-inorganic perovskites, the most extensively studied and used as active materials are the three-dimensional (3D) systems. Their general formula is AMX_3, where A is a light monovalent cation [typically: $CH_3NH_3^+$ (MA), $HC(NH_2)_2^+$ (FA), or $C(NH_2)_3^+$ (GA)], M is a divalent metallic cation (predominantly Pb^{2+} but also Ge^{2+}, Sn^{2+} or Mn^{2+} have been employed) and X is a monovalent halide anion (X=Cl, Br, I). Within their crystal structures, the M^{2+} cations are coordinated by six halides, giving rise to a three-dimensional network of corner-sharing MX_6 octahedra, where the A cations are confined within the cuboctahedral cavities originated by eight octahedra located at the vertices of a primitive cubic lattice.[14,16,17] This means that, in order to form the 3D perovskite structure, the A cation must be small enough so it can fit inside the inorganic octahedral cage while preserving the 3D framework. Goldschmidt's tolerance factors[18] and their influence on structural and functional properties have been widely discussed[19] and recently revised.[20–22] When a larger A cation is employed, the 3D structure breaks to allow its insertion between octahedra, which is often followed by a subsequent reduction in the dimensionality of the system, resulting in two-dimensional (2D) or even one-dimensional (1D) systems. These "perovskitoid" crystal phases are no longer perovskites, though the latter term has been used in a pervasive manner, and for sake of simplicity also used in the following. The structure of 2D perovskites is indeed partially related to that of their 3D counterparts; in the cases which are relevant for the present work, it consists of the alternation of inorganic sheets of MX_6 octahedra with organic layers of a bulky ammonium-based cation, known as barrier or spacer.[23] Differing from the 3D systems, the 2D perovskites exhibit wider band gaps and lower carrier mobilities, which make them less appropriate to play the role, for instance, of the light harvester in a solar cell.[24,25] However, the presence of the larger organic spacers significantly raises the stability of 2D perovskites against ambient conditions, namely: light, heat and, fundamentally, moisture,[26,27] which are the main concern of their 3D analogues.[28] Worthy of note, the thermodynamic stability of the 3D perovskites, in a few cases, is dramatically lowered by accessible transformation paths to insulating materials, such as

[a] Dr. G. García-Espejo, Dr. K. F. Konidaris, Dr. P. Anzini, Prof. S. Brenna, Prof. N. Masciocchi
Dipartimento di Scienza e Alta Tecnologia and To.Sca.Lab
Università dell'Insubria
via Valleggio 11, 22100 Como (Italy)
E-mail: konstantis.konidaris@uninsubria.it
norberto.masciocchi@uninsubria.it
[b] Dr. A. Guagliardi
Istituto di Cristallografia and To.Sca.Lab
Consiglio Nazionale delle Ricerche
via Valleggio 11, 22100 Como (Italy)

Supporting information for this article is available on the WWW under https://doi.org/10.1002/ejic.202300282

Research Article
doi.org/10.1002/ejic.202300282

the δ-phases of $CsPbI_3$[29] and $FAPbI_3$.[30] Therefore, a logical solution is to combine both small and long organic cations, aiming to merge the excellent photophysical properties of the 3D perovskites with the great stability of the 2D ones, an approach which has recently been intensely studied.[16,23,31–35]

Among the resulting intermediate states that can be obtained following this strategy,[36] Ruddlesden-Popper[37] (RP) and Dion-Jacobson[38] (DJ) phases are those that have been more widely explored. Layered perovskites typically consist of 2D slabs of the AMX_3 type structure which are separated by interlayer species and are formulated as $A'_2A_{n-1}M_nX_{3n+1}$ and $A''A_{n-1}M_nX_{3n+1}$, for RP and DJ systems, respectively (where A′ are monocations and A″ dication-based spacer molecules, A is a smaller organic or inorganic cation, M is a divalent metal, and X is a halogen, while *n* represents the number of inorganic octahedra layers, i.e., the thickness of perovskite slabs).[39] As can be inferred from their stoichiometries, the most remarkable structural difference between these two classes of systems is the presence of one (RP) or two (DJ) (charged) ammonium groups in the organic cations and on the subsequent organization of the latter as either a bilayer or a single layer, respectively. This implies that, in the RP systems, the bilayer of the insulating barriers placed between 3D domains is held together through van der Waals interactions, while, in the DJ phases the inorganic slabs are connected by one single dication through electrostatic forces.[40] Since ionic interactions are known to be stronger than the van der Waals ones,[41,42] it follows that the layered structure will be more rigid in the DJ systems, suggesting a superior charge transport and an enhanced performance of the optoelectronic device in which the material could be implemented as the active layer.[34] Examples of 2D lead halide perovskites are nowadays ubiquitous,[43,44] and the materials isolated by combining relatively large "aspherical" organic cations (e.g. butylammonium or phenylethylammonium)[45] or dicationic moieties (e.g. α,ω-pentyl or hexyl-diammonium)[46] provide representative cases.

Motivated by the influence of low-dimensional DJ systems on the progress of perovskite-based optoelectronics, our attention has been focused on the organic molecule 1,4-xylylenediamine. When fully protonated, the simultaneous presence of two ammonium groups makes it suitable as embedded spacer in the organic portion of DJ phases; furthermore, the existence of relatively mobile π-electrons on the aromatic ring can improve the charge transport between organic-inorganic stacks.[47] In its dicationic form [1,4-xylylenediammonium, pXDA], also known as 1,4-bis(ammoniumomethyl)benzene, α,α′-diammonium-*p*-xylene and, as per IUPAC guidelines, [4-(ammoniummethyl)phenyl] methanammonium, has been previously employed for the construction of 2D iodoplumbates[48] and, very recently, also in the preparation of 2D bromoplumbate analogues, to be used as broad light emitters.[49] These species, which are active materials in solar cells and LED devices,[40,50,51] lack a comprehensive structural, thermal and spectroscopic study of the pristine lead-based systems (in both powder and thin-film form). To fill this gap, in this article we report the preparation and complete characterization of the low-dimensional phases obtained by means of simple synthetic processes in which the pXDA species is mixed with a Pb(II) precursor in concentrated HX acids (X=Cl, Br, I). The study explores several features of the phases synthesized as crystalline powders, comprising an exhaustive description of the crystal structures, their optical properties, and their thermal behavior (stability and thermal expansion). Specifically, the detailed thermal response of these materials has been determined, as the use of (intergrown or epitaxial) 2D systems in combination with 3D perovskites, recently proposed for device stability enhancement,[52–54] require similar thermal responses, to avoid detrimental effects, e.g., for day-night temperature cycling.[55,56] Additionally, the synthesized haloplumbates have been prepared as solution-processable thin films and an in-depth study was carried out to investigate their variable characteristics, such as optical properties, morphology, hydrophobicity, stability, and textural effects.

Results and Discussion

Syntheses

In the search for new DJ systems, several attempts with pXDA as the organic barrier were carried out by considering the $(pXDA)PbBr_4$ phase as a scaffold to build structures with $n > 1$. Nevertheless, following synthetic routes based on precipitation methods (like those described in the experimental section) did not lead to the formation of any of the sought $n > 1$ phases, regardless of the organic ammonium/iminium species tested (MA, FA and GA) as a proxy for the A cation. On the contrary, all experiments led to the formation of the $n = 1$ $(pXDA)PbBr_4$ species. Considering the unsuccessful isolation of $n > 1$ DJ crystal phases and aiming at reducing the large energy band gap observed in $(pXDA)PbBr_4$ (*vide infra*) towards applications in optoelectronics, we tackled a doping process by adding iodide ions to the reaction mixture. Since the pristine pXDA iodoplumbate crystallizes in a 1D (and not 2D) polymer, the amount of I^- ions was deliberately kept low. Such doping is expected to lower the energy band gap of the original $(pXDA)PbBr_4$, as the valence band maximum (VBM) of these hybrid haloplumbates is partly composed of *n*p states of the halides present in the crystalline structure. Our synthetic attempts resulted in the isolation of mixed halide 2D systems $(pXDA)Pb(Br_{1-x}I_x)_4$ where $x < 0.1$ (evidence by quantitative X-ray fluorescence analysis). The addition of iodide anions in higher molar ratios provided multiphase powders containing the 1D $(pXDA)Pb_2I_6 \cdot 2H_2O$ phase. The predominant formation of the 1D phase should not surprise; indeed, it has already been reported that, in the presence of water, the dicationic form of pXDA favors the formation of 1D perovskitoid structures.[57] For this reason, Grätzel and co-workers have successfully isolated the 2D $(pXDA)PbI_4$ phase (in its dehydrated form) using a "dry" solid state (mechanochemical) synthesis and demonstrated that the 1D perovskitoid compound (of $(pXDA)Pb_2I_6 . 2H_2O$ formula) can actually be obtained from the degradation of its 2D $(pXDA)PbI_4$ counterpart.[57] Worthy of note, the synthesis of $n > 1$ phases for

Research Article
doi.org/10.1002/ejic.202300282

2D (pXDA)PbI_4 is reported to eventually be accomplished by incorporating methylammonium (MA) or formamidinium (FA) cations and leading to crystalline materials formulated as (pXDA)(MA)Pb_2I_7 and (pXDA)$(FA)_{0.5}(NH_4)_{0.5}Pb_2I_7$ (n = 2).[48]

Crystal Chemistry

(pXDA)$PbCl_4$ crystallizes in the orthorhombic space group *Pbnm*, with the Pb(II) ion located at the cell origin (of -1 point symmetry) and all other atoms lying in general positions. Therein, polymeric chloroplumbate layers, built by corner sharing $PbCl_6$ octahedra, run parallel to the *ab* plane (see Figure 1a). These (one octahedron thick) $\left[PbCl_4^{2-}\right]_\infty$sheets (of *P4/mbm* layer-symmetry) are separated by the pXDA cations, oriented in such a way that their charged portions (the protonated amino residues) point toward the terminal chlorides of the polyanions (not shown here). The planes defined by the Pb ions and the equatorial Cl are found to be 12.48 Å from each other (see Figure 1a). The intermetallic (non-bonding) Pb···Pb distance, of 5.52 Å, is slightly lower than the average value of 5.61 Å for the $(\mu_2\text{-}Cl)_4Pb_4$ fragments of corner-sharing octahedra within monolayer sheets retrieved from the CSD, which, however, fall in a fairly wide range (5.43–5.91 Å). The fact that

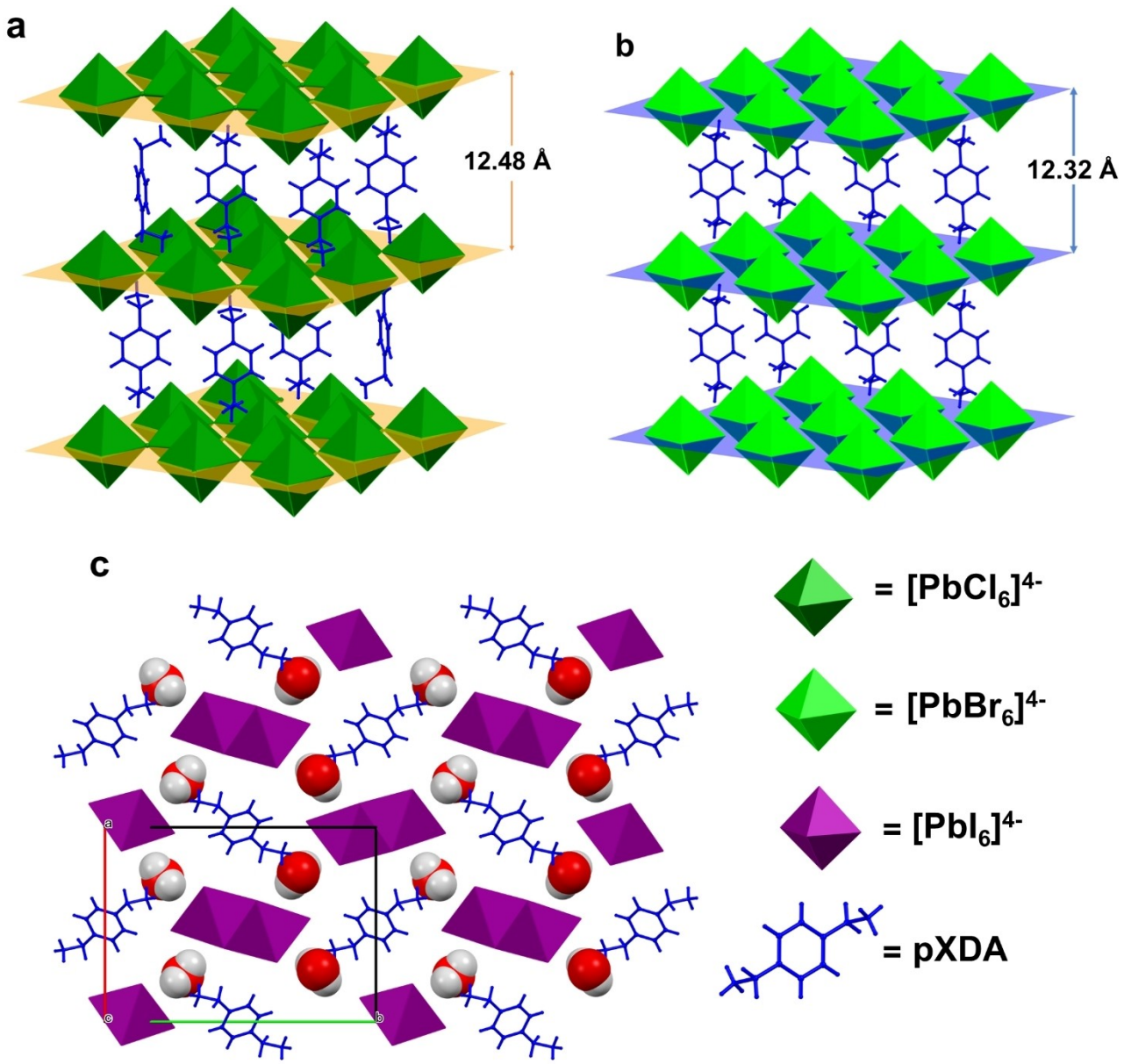

Figure 1. Packing diagram of the crystal structures of a) (pXDA)$PbCl_4$ b) (pXDA)$PbBr_4$ and c) (pXDA)$Pb_2I_6 . 2H_2O$ with Pb(II) ion coordination highlighted in polyhedral representation. A polymeric sheet of corner-sharing octahedra is present in (pXDA)$PbCl_4$ and (pXDA)$PbBr_4$, while, in the (pXDA)$Pb_2I_6 . 2H_2O$ species, infinitely long rodlike $\left[PbI_3^-\right]_\infty$ anions, with edge-sharing octahedra, exist. The H_2O molecules are designed as spacefill models. Color codes: hydrogen (white), carbon (grey), nitrogen (blue), oxygen (red), chloride (green), bromine (brown) and iodine (violet).

terminal (here, axial) Pb–Cl distances are not significantly shorter than μ_2-Cl bridging ones (see Table 1) was initially suspicious; nevertheless, this is also true for the structural analogues retrieved in the CSD database. We also note that the bridging chlorides in (pXDA)$PbCl_4$ are not symmetrically linked to the adjacent Pb ions (Pb–Cl distances of 2.83 and 2.92 Å). This unexpected observation finds a strong confirmation in the crystal structure of $(C_4H_4N_2)PbCl_4$,[58] where shorter (avg. 2.82 Å) and longer (avg. 2.91 Å) values are observed. Similar evidence can be found in other analogues [e.g., in the isomeric $(C_6H_{10}N_2)$-$PbCl_4$ phases[59,60]] and might be attributed to the non-spherical shape of the Pb^{II} ion, due to incipient and underestimated stereochemical activity of the 6 s^2 valence orbital.[61]

We also comparatively discuss here the structure of the already known phase (pXDA)$PbBr_4$,[49] which crystallizes in the monoclinic space group $P2_1/a$, but it is closely related to that of its lighter analogue. Again, the Pb^{II} ion is located at the cell origin and all other atoms lie in general positions. If allowance for the change of the β angle from 91.0 to exact 90° is given and the **c** axis is halved, then the two structures can be considered nearly equivalent (see Figure 1b), with the obvious inflation of the molar volume (V/Z = 373 and 410 $Å^3$ for (pXDA)-$PbCl_4$ and (pXDA)$PbBr_4$, respectively). Here, the distance between two $\left[PbBr_4^{2-}\right]_\infty$ layers (12.32 Å) is slightly shorter than that observed for the chloro-analogue (see Figure 1b). Differently from the chloroplumbate case, for (pXDA)$PbBr_4$, as well for the analogous species containing $\left[PbBr_4^{2-}\right]_\infty$ sheets, dyssimmetrization of the Pb–Br distances within the Pb–Br–Pb fragments is not observed. Beyond interatomic distance changes (see Table 1), another subtle difference between the chloride and the bromide derivatives can be spotted. In (pXDA)$PbCl_4$, the pXDA molecules are bisected by mirror planes, while in (pXDA)-$PbBr_4$, they sit on an inversion center. This makes the pXDA cations in the former case possess a *syn*-conformation of the branching CH_2NH_3 residues, while the *anti*-conformation is present in the latter one. Though slightly disfavored *per se* by electrostatics (in gas phase), a few occurrences of the *syn* conformer in crystalline species appeared in the literature, accounting for a mere 7% of the overall cases. Worthy of note, this similarity may suggest facile interconversion to isomorphous phases if additional conformational freedom is allowed, for example through heating (*vide infra*). In addition, for all the 2D (pXDA)PbX_3 species (X=Cl, Br, I), the degree of relative displacements of neighboring perovskite layers, quantitatively evaluated by using Marchenko et al. approach,[62] ends up in (t_1,t_2) parameters of (0,0), (0,0.027) and (0,0.021), respectively. Fully or substantially eclipsed layers are then present in these materials. According to the original paper, such eclipsed configuration is also associated to the lowest achievable band gaps, making them prone to both electronic conduction and efficient solar spectrum absorption.

While the crystal structures of the Cl and Br derivatives share the common feature of infinite sheets based on corner-sharing octahedra, separated by slabs of organic dications, the iodide analogue, of markedly distinct stoichiometry, could only be precipitated in the form of (pXDA)$Pb_2I_6 \cdot 2H_2O$ (*i.e.* in a non-perovskitic $A_{1/2}BX_3$ structure, with A = doubly charged moiety). Specifically, (pXDA)$Pb_2I_6 \cdot 2H_2O$ crystals are monoclinic, $P2_1/n$, and contain infinite rods of $\left[PbI_3^-\right]_\infty$ formulation (and $P112_1/m$ rod-group symmetry), generated by edge-sharing octahedra hinged about μ_3-iodides (see Figure 1c). Within each polyanion, terminal and μ_2-bridging iodides also exist. In (pXDA)-$Pb_2I_6 \cdot 2H_2O$, the organic dications are in the (more common) *anti*-conformation, and water molecules are placed in the crystal interstices, making an extensive network of hydrogen bonds involving charged RNH_3^+ residues and iodine anions. In particular, the crystal structure of the high-temperature (pXDA)-Pb_2I_6 crystal phase (see Supporting Information) is also monoclinic, $P2_1/n$, with the **a** axis and the β angle slightly expanded, and the **b** axis length significantly contracted. The main features of the polymeric $\left[PbI_3^-\right]_\infty$ rods are maintained, and relevant structural features, such as Pb–I bond distances and Pb–I–Pb bond angles, are basically unchanged. This also explains why this material, once cooled in air to RT, easily restores the hydrated form, sucking moisture from the environment.

As a final comment to our structural discussion, we highlight that the main geometrical features (bond distances and angles) of these species well agree in both X-ray powder

Table 1. Synoptic collection of the most relevant geometrical parameters, together with the experimentally determined optical band gaps. Bold characters refer to the (pXDA)Pb_2I_6 anhydrous crystal phase, measured at 170 °C. The values in parentheses are the average values determined from a CSD search.

Parameter	(pXDA)$PbCl_4$	(pXDA)$PbBr_4$	(pXDA)$Pb_2I_6 \cdot 2H_2O$
Topology	2D layer/square mesh corner-sharing octahedra	2D layer/ square mesh corner-sharing octahedra	1D-ribbon, edge-sharing octahedra
Pb…Pb [Å]	5.52 (5.61)	5.77 (5.84) *5.77*[a]	4.59–4.57 4.72–4.72 4.72
Pb-X_{term} [Å]	2.88 (2.87)	2.99 (3.00) 3.01	3.03–3.05 3.15
Pb-X_{bridg} [Å]	2.87 (2.89)	2.97 (3.01) 2.99	3.16–3.32[b] 3.18–3.21 3.17–3.43
Pb-X_{bridg}-Pb [°]	148.2 (159.1)	150.1 (157.2) 150.2	93.3–90.4[b] 92.4–88.3 97.7–88.3
Optical band-gap [eV]	3.58	2.96	2.86

[a] Values in *italics* from refs. [48] and [49] [b] μ_2 and μ_3-I, respectively.

Research Article
doi.org/10.1002/ejic.202300282

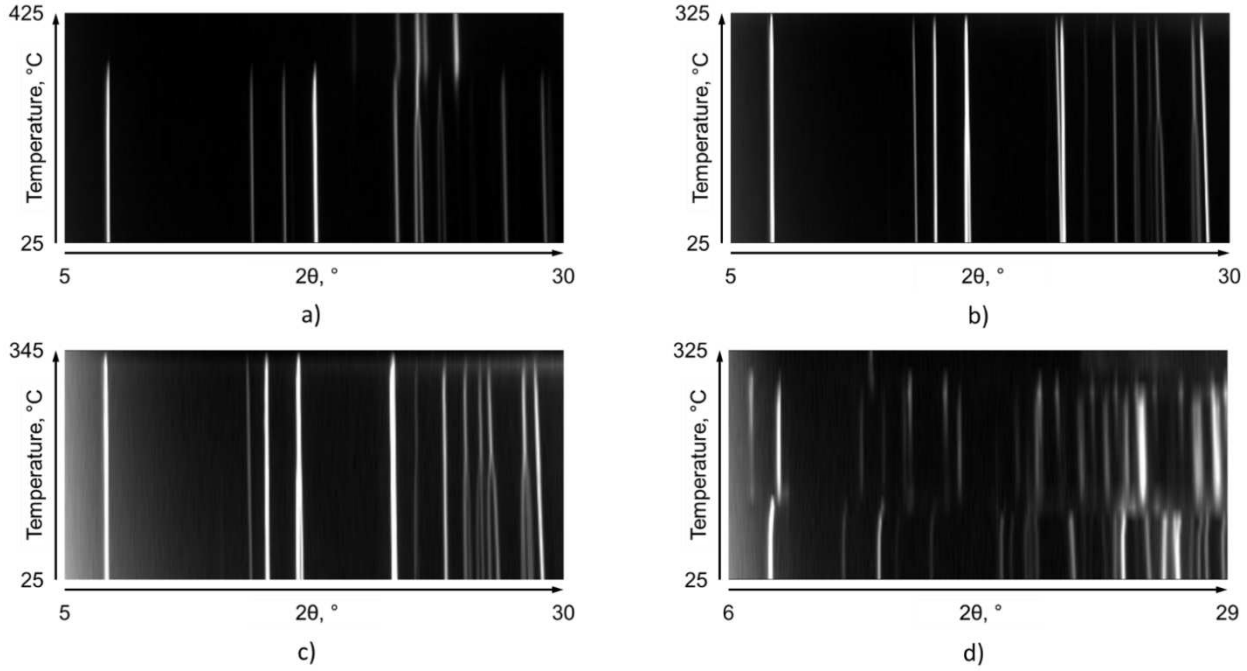

Figure 2. VT-XRD plots for a) (pXDA)$PbCl_4$, b) (pXDA)$PbBr_4$, c) (pXDA)$Pb(Br_{0.9}I_{0.1})_4$ and d) (pXDA)$Pb_2I_6 . 2H_2O$. Horizontal axis: 2θ,°; vertical axis: T, °C. The listed temperatures are those measured by a thermocouple set at the bottom of the aluminum sample holder and are not those of the surface of the samples. Indeed, due to thermal gradients for samples exposed to air, broad interval ranges and diffraction peak widening are expected.

diffraction (XRPD) and single crystal diffraction (SXD) studies. Highly comparable values are indeed reported in Table 1, where the synoptic collection of these parameters (normal and *italicized* fonts) differ, at most, by 0.02 Å and 2°. Consequently, as the (pXDA)$PbCl_4$ species was not characterized by conventional SXD, we can safely state that the XRPD results can be considered fully reliable.

Thermal Characterization

The as-prepared powders of all precipitated haloplumbates were studied by variable temperature X-ray diffraction (VTXRD) analysis and manifested interesting modifications upon raising the temperature until decomposition, typically occurring well above 250 °C. Figure 2 shows the thermodiffractograms of the four species (including the mixed-halide one), where phase changes can be visually appreciated by discontinuities at a given temperature. Linear thermal expansion coefficients, determined from the cell variations illustrated in Figure 3, are reported in Table 2, together with the derived thermal strain eingenvectors and their orientations with respect to cell axes. Thermogravimetric and DSC traces are shown in Figure 4. The values of the thermal expansion coefficients, falling roughly in the 10–40 MK^{-1} range, are comparable to those of the 3D inorganic and hybrid lead halide perovskites ($APbX_3$, with A═Cs, MA and FA, and X═Cl, Br and I)[63] and, as such, are fully compatible for the preparation of stable intergrown or epitaxial

Table 2. Linear thermal expansion coefficients (MK^{-1}) for cell axes, angles and volume. The principal strain eigenvalues (E_i, i = 1,2,3, representing the thermal expansion coefficients along the principal axes) and the φ angles of the corresponding eigenvectors with the a, b, c axes, computed for a 100 °C increase from room temperature, are also reported.

Species	(pXDA)$PbCl_4$	(pXDA)$PbBr_4$	(pXDA)Pb$(Br_{0.9}I_{0.1})_4$	(pXDA)Pb_2I_6 $2H_2O$
κ_a	15	36	22	−11
κ_b	30	27	24	25
κ_c	27	8	46	42
κ_β		−11	−22	−48
κ_V	73	72	94	67
E_1	16	12	14	−16
E_2	28	17	26	15
E_3	30	40	57	43
ϕ_{E1}(a,b,c) [°]	0,90,90	90,0,90	166,90,64	155,90,58
ϕ_{E2}(a,b,c) [°]	90,90,0	159,90,69	90,0,90	90,0,90
ϕ_{E3}(a,b,c) [°]	90,0,90	69,90,21	65,90,26	65,90,32

Research Article
doi.org/10.1002/ejic.202300282

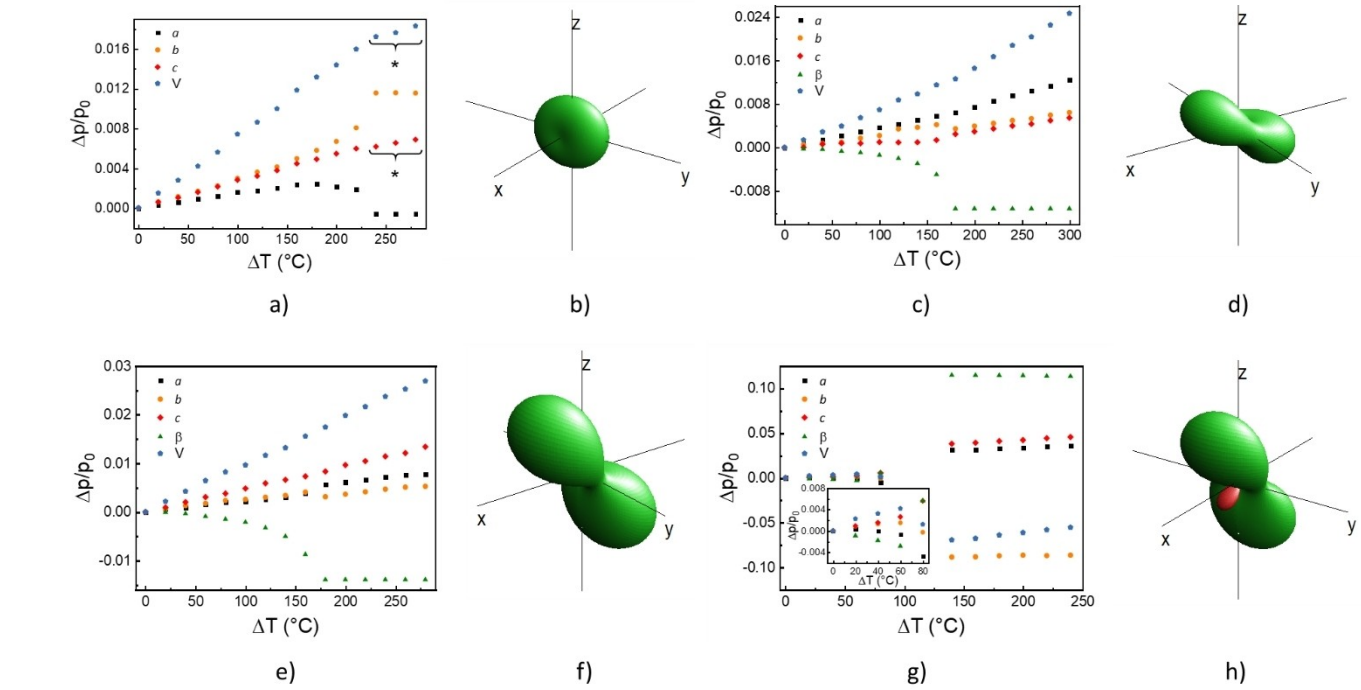

Figure 3. The thermal evolution of the lattice parameters, expressed as $\Delta p/p_0$ (see text) and the visualization of the strain tensors derived therefrom. a, b): (pXDA)$PbCl_4$.c, d): (pXDA)$PbBr_4$.e, f): (pXDA)$Pb(Br_{0.9}I_{0.1})_4$.g, h): (pXDA)Pb_2I_6.$2H_2O$. The points marked with an asterisk in a) were calculated by duplicating the values of the lattice parameters **c** and V obtained for β-(pXDA)$PbCl_4$ in order to show a clearer comparison after the phase transition.

layers of (pXDA)PbX_4 onto 3D $APbX_3$ materials.[64] Indeed, it would appear especially worrisome if the thermal expansion coefficient of an epi-layer was significantly different from the substrate, as this would cause a material stress under repeated temperature cycling, with detrimental effects in crystal/grain size and shape, e.g., in solar cell devices in normal day-night operation.

The (pXDA)$PbCl_4$ and (pXDA)$PbBr_4$ species, and the partially I-doped one, manifest low (orthorhombic or monoclinic) symmetry at RT, eventually raised to tetragonal above 150 °C, obtained by minimal atomic shifts. The wishbone-shaped merging of some (originally distinct) reflections pictorially witnesses this structural change (more evident in Figure 2c). Additionally, in the studied temperature range, the (pXDA)$PbCl_4$ phase shows another thermally induced transformation, starting at ca. 250 °C, and attributed to sample decomposition, which, for the Br-containing samples, occurs at much higher temperature. (pXDA)Pb_2I_6.$2H_2O$, which is chemically and structurally different,[57] follows a significantly different transformation path: above 150 °C it transforms into an anhydrous HT-phase, through a *reversible* reaction. The change of the XRPD pattern from the hydrated to the anhydrous phase is also very evident (see Figures 2d and 3g).

Worthy of note, reversibility of the dehydration process was found to be only partial. We attribute this fact to hydration kinetics upon cooling (performed at environmental relative humidity values in the 50–70 % range), where the inner part of the crystals in the powder is shielded by the external re-hydrated shell. Alternatively, since for a hydrated-to-anhydrous reaction ($H \rightarrow A + nH_2O$) the equilibrium constant reads as $K_{eq} = p^n_{H2O}$, thermodynamic effects could have also played a significant role, but this aspect was not further investigated. Moreover, hydration of a similar compound, the 2D (pXDA)PbI_4 phase,[48] isostructural to the Cl and Br species, was reported to form the same hydrated compound of 1D chain topology, (pXDA)Pb_2I_6.$2H_2O$ (isolated by us as pure phase in quantitative yields), through elimination of the (pXDA)I_2 salt.[57]

Thin Film Characterization

Grazing Incidence X-ray Diffraction (GIXRD) measurements of thin films

The 2D-GIXRD images of two spin-coated films of nominal (pXDA)$PbBr_4$ and (pXDA)Pb_2I_6 composition, exhibit several arc-shaped traces of uneven intensity and a perfect symmetry with respect to the central vertical line (Figures S1 and S2). After

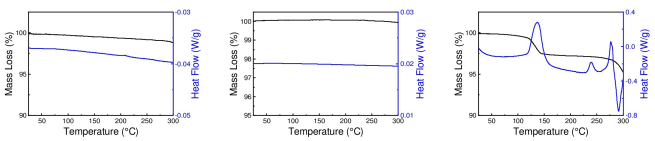

Figure 4. The thermogravimetric (black) and differential scanning calorimetric (blue) curves for (pXDA)$PbCl_4$ (left), (pXDA)$PbBr_4$ (middle) and (pXDA)-Pb_2I_6.$2H_2O$ (right) phases.

Research Article
doi.org/10.1002/ejic.202300282

transformation into ψ, q polar maps (Figures S3 and S4), one can easily recognize that the formed films fully match the structure of (pXDA)$PbBr_4$ and (pXDA)$Pb_2I_6.2H_2O$ phases found in the original bulk materials and that the angular intensity distributions along ψ is indicative of partially textured films. The analysis of the ψ profiles of the 001 and 200 peaks (for (pXDA)$PbBr_4$ and (pXDA)$Pb_2I_6.2H_2O$, respectively) indicates that both films tend to preferentially orient along one specific direction with respect to the normal to the substrate surface (Figure 5). Film mosaicity for (pXDA)$PbBr_4$ is definitely lower ($fwhm_{001} = 7.4°$) than for (pXDA)$Pb_2I_6.2H_2O$ ($fwhm_{200} = 19.4°$), in full agreement with the expected structural/morphologic correlation dominated by the 2D layers present in the former. Indeed, the (001) preferential orientation for (pXDA)$PbBr_4$ is easy to interpret, as it nicely matches the stacking of the infinite 2D inorganic layers within the monoclinic crystals (of pseudotetragonal metrics). A little more surprising is the (200) pole for (pXDA)$Pb_2I_6.2H_2O$, which we however found to be related to the real-space direction where H-bond interactions between are scarce(r).

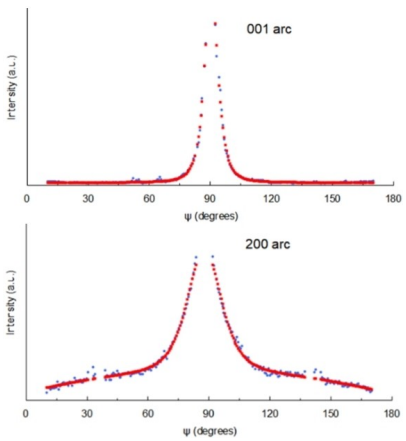

Figure 5. The intensity distribution of the 001 and 200 reflections for (pXDA)$PbBr_4$ (top) and (pXDA)$Pb_2I_6.2H_2O$ (bottom) (in the film) showing a much narrower peak at $\psi = 90°$ ($fwhm = 7.4°$) for (pXDA)$PbBr_4$ than for (pXDA)$Pb_2I_6.2H_2O$ ($fwhm = 19.4°$).

Contact angle and stability measurements

The hydrophilicity /hydrophobicity character of the prepared perovskite thin films for (pXDA)$PbBr_4$ and (pXDA)Pb_2I_6 was studied with contact angle (CA) measurements (shown in Figure 6a–d). The contact angle of the water droplet on the (pXDA)$PbBr_4$ film is found to be 54.3°, while that on (pXDA)-$Pb_2I_6.2H_2O$ shows decreased wetting (CA = 74.7°) and therefore higher hydrophobicity. These values are in agreement with those previously reported for similar pXDA-containing perovskite thin films.[51]

For reference, contact angle measurements for the underlying quartz substrate surface (78.1°) as well as for commercial teflon solid disk (86.9°) were also carried out. Worthy of note, after removing the probe droplet, an evident footprint

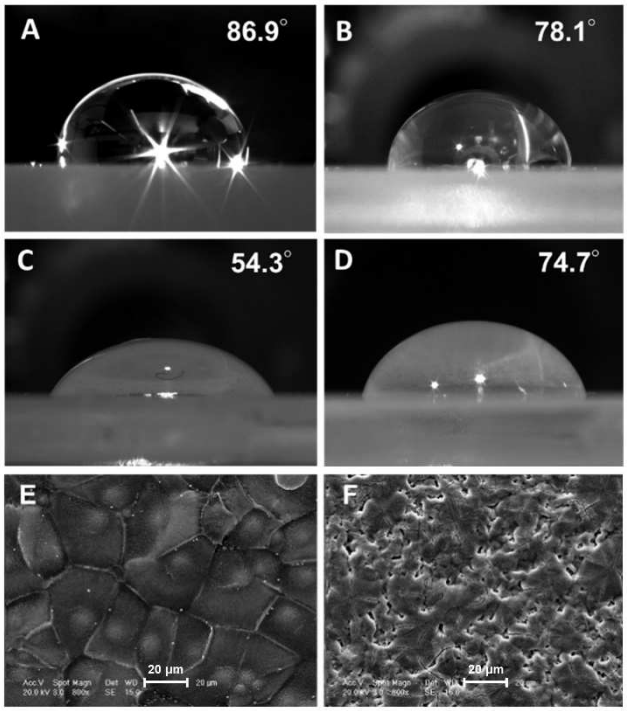

Figure 6. Static contact angle measurements of a droplet of water on (A) Teflon, CA = 86.9°, (B) fused quartz, CA = 78.1° (C) thin film of (pXDA)$PbBr_4$ on fused quartz, CA = 54.3° and (D) thin film of (pXDA)Pb_2I_6 on fused quartz, CA = 74.7°. In panels (E) and (F), top-view SEM images of (pXDA)$PbBr_4$ and (pXDA)Pb_2I_6 perovskite thin films, respectively.

appeared on the tested surfaces, indicating that some dissolution of the original films occurred when put in contact with water for 1 h. To test its environmental stability, the thin film of (pXDA)$PbBr_4$ was exposed to ambient conditions and its XRD trace was monitored over a period of six months, no noticeable difference being observed (Figure S5).

SEM imaging. The surface morphology of the perovskite thin films was investigated by means of scanning electron microscopy (SEM, see Figure 6e&f). For (pXDA)$PbBr_4$, grains with sizes > 20 μm were observed, displaying a morphology similar to other pXDA lead perovskites (with n = 1).[51] On the thin film of (pXDA)$Pb_2I_6.2H_2O$, the grains are found to be of only a few micrometers, depicting smaller crystallite size for the 1D material.

Diffuse reflectance measurements of the bulk powders

The optical band gap (E_g) values of (pXDA)$PbCl_4$, (pXDA)$PbBr_4$, (pXDA)$Pb_2I_6.2H_2O$ and pXDA)$Pb(Br_{1-x}I_x)_4$ were calculated from their corresponding Tauc plots (see Figure 7). Among the four studied species, the mixed halide 2D perovskite [(pXDA)Pb-$(Br_{1-x}I_x)_4$], displays the lowest band gap (2.72 eV); while the E_g value of the 1D species, (pXDA)$Pb_2I_6.2H_2O$, is slightly higher (2.86 eV). The E_g values of (pXDA)$PbBr_4$ and (pXDA)$PbCl_4$ are 2.96 eV and 3.58 eV, respectively, and follow the anticipated trend of Cl > Br > I. Similarly, that lead iodide 1D perovskites

Research Article
doi.org/10.1002/ejic.202300282

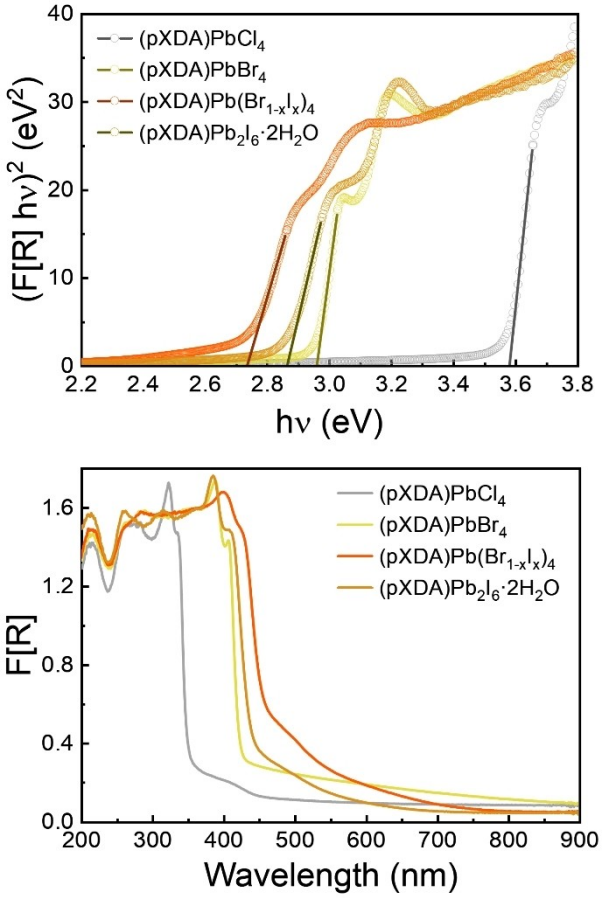

Figure 7. The Kubelka-Munk transformed UV-Vis diffuse reflectance spectra for the four species stable at RT (bottom) and the derivation of the optical band gaps by the Tauc plot procedure (top).

display larger band gaps than their 2D counterparts is also not unexpected.[65]

UV-Vis and PL measurements of thin films

Aiming at further investigating the optoelectronic properties of these species, the UV-Vis absorption and steady-state photoluminescence (PL) spectra were recorded at room temperature for the two prepared perovskite thin films (Figure 8). In the absorbance spectrum of the (pXDA)$PbBr_4$ thin film, a maximum at ~400 nm is observed, as previously reported for other 2D lead bromides.[66] Upon excitation at 400 nm, the obtained PL spectrum did not contain any peaks attributed to the perovskite material. On the contrary, if the excitation wavelength is lowered to 355 nm, a relatively strong emission centered at 420 nm is observed, with a non-negligible Stokes shift of ~0.147 eV. This finding is in accordance with the data previously reported for its corresponding powder specimen,[49] suggesting that the emission is size and morphology independent. At variance, the thin film of the 1D phase, (pXDA)$Pb_2I_6.2H_2O$, does not show measurable PL.

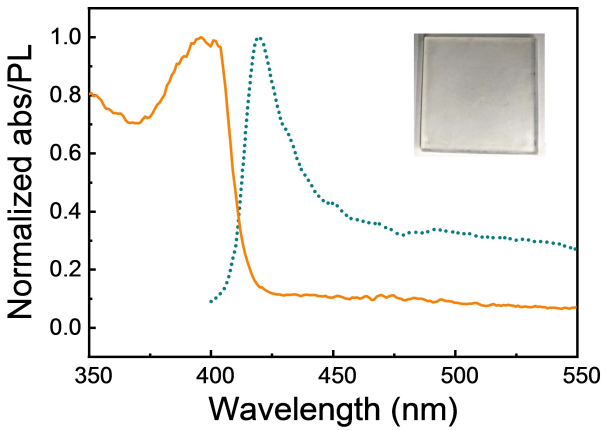

Figure 8. Normalized UV-Vis absorption spectrum (solid line) and steady-state PL spectrum (exc. 355 nm) (dashed line) of a (pXDA)$PbBr_4$ perovskite thin film deposited on fused quartz and recorded at room temperature. Inset: Image of the perovskite thin film.

Conclusion

Herein we presented a comprehensive study of the Pb^{II}/pXDA/X^- (X=Cl, Br, I) system series, which led to the isolation of two 2D Dion-Jacobson phases, formulated as (pXDA)PbX_4 (X=Cl, Br). Attempts to isolate the homologous 2D iodo-based structure were not successful, as the 1D non-perovskitic crystal phase, (pXDA)$Pb_2I_6.2H_2O$, systematically formed. Nevertheless, partial replacement of bromine with iodine ions in (pXDA)PbX_4 was attained, resulting in the formation of the mixed halide 2D perovskite (pXDA)$Pb(Br_{1-x}I_x)_4$. For a minimal doping (x = 0.10), a significant 0.26 eV red-shift of the optical band gap was observed. The thermal behavior and material stability was studied by DSC, TGA and VT-XRD measurements, showing that the 2D species are stable in air up to 250 °C, while (pXDA)-$Pb_2I_6.2H_2O$ *reversibly* dehydrates slightly above 120 °C, forming a crystalline (pXDA)$Pb_2I_6.1D$ phase. Thin films were prepared by spin-coating DMSO solutions of the (pXDA)PbX_4 and (pXDA)-$Pb_2I_6.2H_2O$ species on polished fused quartz substrates. Synchrotron-based GIXRD analysis showed that both films possess a pronounced texture, larger in the 2D (pXDA)$PbBr_4$ perovskite (001 pole) than in the 1D (pXDA)$Pb_2I_6.2H_2O$ species (200 pole). UV-Vis spectral properties of both bulk powders and thin films were also assessed, demonstrating that (pXDA)$PbBr_4$ films (but not those of (pXDA)$Pb_2I_6.2H_2O$) are PL active and display a non-negligible Stokes shift of ca. 0.15 eV.

Experimental Section

Materials. Lead oxide (PbO, 99.9%), 1,4-xylylenediamine (pXDA: $C_6H_4(CH_2NH_2)_2$, >98%), hydrobromic acid (HBr, 48% w/w in H_2O) and hydroiodic acid (HI, 57% w/w in H_2O) were purchased from Sigma-Aldrich/Merck. Hydrochloric acid (HCl, 37% w/w in H_2O) was purchased from VWR Chemicals. All reagents were used as received without any further purification.

Syntheses

(pXDA)PbCl$_4$. PbO (0.5 mmol, 0.112 g) was dissolved in 4 mL of HCl solution by stirring and heating the mixture up to 70 °C. Subsequent addition of solid pXDA (0.25 mmol) caused the immediate precipitation of a white solid. Attempts to redissolve the precipitate under vigorous stirring and heating up to the solution boiling point were unsuccessful. Therefore, stirring was discontinued and the solution was left to slowly cool to room temperature. After a few hours, a polycrystalline solid was collected and dried by filtration under vacuum.

(pXDA)PbBr$_4$. Solid pXDA (0.2 mmol, 0.027 g) was dissolved in 4 mL of a HBr solution by stirring and heating the mixture up to the solvent boiling point. Subsequent addition of PbO (0.4 mmol, 0.089 g) caused the immediate precipitation of a whitish solid. The precipitate was redissolved under vigorous stirring and heating the solution at boiling conditions. Then, stirring was discontinued and the solution was left to slowly cool to room temperature overnight, during which time a bright white-yellowish precipitate started to crystallize. The obtained polycrystalline solid was collected and dried by filtration under vacuum.

(pXDA)Pb(Br,I)$_4$. Solid pXDA (0.25 mmol, 0.034 g) was dissolved in 4 mL of a hydrohalide acid mixture solution (3.55 mL of HBr and 0.45 mL of HI) by stirring and heating the mixture up to boiling. Subsequent addition of PbO (0.5 mmol, 0.112 g) caused the immediate precipitation of a yellowish solid. The precipitate was re-dissolved under vigorous stirring and heating the solution at boiling conditions. Then, stirring was discontinued and the solution was left to slowly cool to room temperature overnight, during which time a bright yellow precipitate started to crystallize. The obtained polycrystalline solid was collected and dried by filtration under vacuum.

(pXDA)Pb$_2$I$_6$.2H$_2$O. Solid pXDA (0.25 mmol, 0.034 g) was dissolved in 4 mL of a HI solution by stirring and heating the mixture up to boiling. Subsequently, PbO (0.5 mmol, 0.112 g) was added and remained undissolved until its dissolution by heating solution at boiling conditions under vigorous stirring. Once a clear solution was obtained, stirring was discontinued and the solution was left to slowly cool to room temperature overnight, during which time a bright yellowish precipitate started to crystallize. The obtained polycrystalline solid was collected and dried by filtration under vacuum.

(pXDA)Pb$_2$I$_6$. By heating (pXDA)Pb$_2$I$_6$.2H$_2$O above 150 °C, dehydration occurs, partially reversible in nature. The new anhydrous phase, (pXDA)Pb$_2$I$_6$, was thus prepared by heating the hydrate at 170 °C in neat conditions and, to prevent easy rehydration from environmental conditions (with typical RH in the 50–70% range), the polycrystalline solid was studied directly in the diffractometer heating stage, which enabled the full structural characterization discussed below.

Caution. Even though no problem was ever encountered in the course of this research, concentrated hydrohalide acids are potentially harmful, both as solutions and as fumes. Since these acids are heated up to boiling during the synthetic process, it is recommended to handle them under a working fume hood. Hence, special attention must be taken when synthesizing the reported pXDA lead halides.

Characterization procedures

Diffuse reflectance spectroscopy. UV-vis-NIR reflectance spectra of the powders were measured in the 200–900 nm range using a UV-2600 Shimadzu spectrometer. $BaSO_4$ was used as non-absorbing reflectance reference. The Kubelka-Munk function F[R] was calculated from the reflectance spectrum, using the $F[R] = (1-R)^2/2R$ relationship. Taking F[R] as the representative of the sample absorbance spectrum, extrapolation of the linear portion of the $(F[R]\ h\nu)^2$ vs $h\nu$ plot on the $h\nu$ axis provided experimentally accessible direct band gap values (Tauc plots).

UV-Vis and PL measurements. The UV-vis absorption and emission spectra of the perovskite thin films were performed using an Edinburgh Instrument FS5 fluorescence spectrophotometer equipped with a 150 W continuous xenon lamp as a light source and were corrected for the wavelength response of the instrument.

X-ray fluorescence. Gently ground powders of the crystalline RT-phases were deposited on a polycarbonate film and analyzed with a MiniPal2 XRF spectrometer (PANalytical), equipped with a Cr-anode operating at 30 kV and 2 μA. X-ray fluorescence lines were measured for Pb (L_α and L_β lines, at 10.5 and 12.6 keV, respectively), Cl (K_α and K_β lines, at 2.6 and 2.8 keV, respectively), Br (K_α and K_β lines, at 11.9 and 13.3 keV, respectively) and I (L_α, $L_{\beta1}$, $L_{\beta2}$ and L_γ lines, at 3.93, 4.22, 4.51 and 4.80 keV, respectively). Intensity calibration for Pb/Cl in (pXDA)PbCl$_4$ was performed using an equimolar amount of Pb and Cl, through a mixture of PbO and CsCl; in this occasion, partial overlap of the K(Cl) and M_α(Pb) emission lines made it difficult to reach high analytical accuracy. To determine the Pb/Br ratio in (pXDA)PbBr$_4$, a pristine $PbBr_2$ powder was used instead of calibration. As for the Pb/I ratio in (pXDA)Pb$_2$I$_6$.2H$_2$O, an equimolar amount of Pb and I was employed, using a physical mixture of co-ground PbO and CuI. Similarly, the ratio among Pb, Br and I in (pXDA)Pb(Br,I)$_4$ was assessed using an equimolar mixture of $PbBr_2$ and CuI as calibrant.

Thin film preparation. Both hybrid materials (pXDA)PbBr$_4$ and (pXDA)-Pb$_2$I$_6$.2H$_2$O were used as obtained from their respective synthesis, without any further treatment. In both cases, powders were dissolved in DMSO at a 1.0 mol L^{-1} concentration. Thin films were prepared by spin-coating 100 μL of the solutions at 1300 rpm for 40 s onto 2.5×2.5 cm^2 GE 124 fused quartz substrates (supplied by Technical Glass Products Inc., Painesville, OH). Immediately afterwards, the substrates were annealed for 30 min at 100 or 150 °C for (pXDA)PbBr$_4$ or (pXDA)Pb$_2$I$_6$.2H$_2$O solutions, respectively, in order to ensure the complete evaporation of the remaining solvent and the formation of the resulting polycrystalline films. Before operation, the quartz substrates were subjected to a cleaning pretreatment, starting with several sequential ultrasonic bath treatments (5 minutes each) in Hellmanex™ solution, deionized water and isopropyl alcohol, followed by blow-drying with a stream of nitrogen gas and finally, a UV-ozone treatment for 10 min (L2002A2 UV Ozone Cleaner, Ossila B.V., Leiden, The Netherlands).

X-ray diffraction analysis. XRPD measurements were performed using a Bruker AXS D8 Advance diffractometer in Bragg-Brentano θ:θ geometry, equipped with a Lynxeye position sensitive detector. DS:0.5°; Generator setting: 40 kV, 40 mA; Ni-filtered Cu-K$_\alpha$ radiation, $\lambda = 1.5418$ Å. XRPD data for structure solution were collected the 3–105° 2θ range for all samples, sampling at 0.02°, with scan time lasting ca. 16 h.

Standard peak search enabled the location of 20 low-angle peaks, typically falling in the 5–27° range, which were then fed to the Singular Value Decomposition[67] indexing algorithm of TOPAS-R, which provided the following results. For (pXDA)PbCl$_4$, Orthorhombic P, a = 24.54, b = 7.75, c = 7.85 Å, GoF(20) = 69.9; for (pXDA)PbBr$_4$, Monoclinic P, a = 14.66, b = 8.15, c = 8.16, β = 122.8°, GoF(20) = 110.6; for (pXDA)Pb$_2$I$_6$.2H$_2$O, Monoclinic P, a = 13.92, b = 19.06, c = 4.58, β = 101.0°, GoF(20) = 41.4. For the reasons discussed below, the determined cells were reduced, or transformed, to facilitate the structural comparisons. Density considerations and systematic absences suggested space groups *Pbnm*, *P2$_1$/a* and *P2$_1$/n* for (pXDA)-PbCl$_4$, (pXDA)PbBr$_4$ and (pXDA)Pb$_2$I$_6$.2H$_2$O, respectively. Structure solution was initiated by the simulated annealing technique using the 5–50° 2θ section only and freely floating Pb and halides (X), with

Research Article
doi.org/10.1002/ejic.202300282

soft restraints on the Pb–X bond distances and a refinable site occupancy factor enabling Pb to approach a symmetry site. Once an approximate model was found for the complex anions, pXDA and, when pertinent, water moieties were added as rigid bodies with idealized geometry (distances, angles), with fixed center of mass location but free molecular orientations and torsions. The final refinements were performed using all data up to 105° 2θ, and the coordinates of lead ions and all halides atoms were treated independently. A small correction for preferred orientation, in the March-Dollase formulation (here, the g_{hkl} parameter), was includes, a single isotropic displacement parameter was assigned to all atoms and the residual (instrumental and sample-dependent) smooth background modeled by a Chebyshev polynomial. All X-ray diffraction-related computations were performed using the TOPAS–R suite of programs.[68] Figure S6 illustrates the final Rietveld refinement plots for all three room temperature species.

Deposition Numbers 2244927 [for (pXDA)$PbCl_4$], 2244928 [for (pXDA)$PbBr_4$], 2244929 [for (pXDA)$Pb_2I_6 . 2H_2O$] contain the supplementary crystallographic data for this paper. These data are provided free of charge by the joint Cambridge Crystallographic Data Centre and Fachinformationszentrum Karlsruhe Access Structures service.

Crystal data for (pXDA)$PbCl_4$: $C_8H_{14}Cl_4N_2Pb$, fw = 487.22 g mol^{-1}, orthorhombic, *Pbnm*, a = 7.8517(1), b = 7.7555(1), c = 24.5260(3) Å, V = 1493.47(4) Å^3, Z = 4, ρ_{calc} = 2.167 g cm^{-3}, μ(Cu–Kα) = 278.5 cm^{-1}; g(001) = 0.94, R_p and R_{wp}, 0.051 and 0.069 respectively, 6.5–105° 2θ range. R_{Bragg} = 0.034.

Crystal data for (pXDA)$PbBr_4$: $C_8H_{14}Br_4N_2Pb$, fw = 665.03 g mol^{-1}, monoclinic, $P2_1/a$, a = 8.1640(1), b = 8.1590(1), c = 12.3233(1) Å, β = 91.017(1)°, V = 820.73(1) Å^3, Z = 2, ρ_{calc} = 2.691 g cm^{-3}, μ(Cu–Kα) = 307.9 cm^{-1}; g(001) = 1.05, R_p and R_{wp}, 0.045 and 0.061 respectively, 6.5–105° 2θ range. R_{Bragg} = 0.028.

Crystal data for (pXDA)$Pb_2I_6 . 2H_2O$:$C_8H_{18}I_6N_2O_2Pb_2$, fw = 1350.07 g mol^{-1}, monoclinic, $P2_1/n$, a = 13.8190(4), b = 19.0778(5), c = 4.5921(2) Å, β = 98.001(2), V = 1198.85(7) Å^3, Z = 4, ρ_{calc} = 3.7e g cm^{-3}, μ(Cu–Kα) = 872.5 cm^{-1}; g(001) = 1.09, R_p and R_{wp}, 0.049 and 0.072 respectively, 7–105° 2θ range. R_{Bragg} = 0.027.

Variable temperature X-ray diffraction (VTXRD) measurements were performed on a Bruker AXS D8 Advance diffractometer, using a custom-made sample heater built by Officina Elettrotecnica di Tenno (Ponte Arche, TN, Italy). Data were collected in step scan mode, with $\Delta 2\theta = 0.02°$, t = 1 s, and 2θ range limited to 30°, measuring the sample under isothermal condition and raising the temperature from room temperature up to decomposition in 20 °C steps. As our heating stage worked in air, the presence of non-negligible thermal gradients cannot be excluded. For (pXDA)Pb_2I_6, a prolonged XRD measurement was performed at 170 °C on a Peltier-controlled sample heater (built by Officina Elettrotecnica di Tenno) equipped with a silicon zero-background plate, to stabilize the high-temperature phase after complete water elimination. Noteworthy, upon cooling to RT, this species reverts to a mixture of metastable phase (pXDA)Pb_2I_6 (reverting, within a few hours at 70% RH, to the hydrated phase), thus preventing a 100% pure-phase XRD data collection at RT. Crystal data for the high-temperature (pXDA)Pb_2I_6 phase are supplied in the Supporting Information. The thermal strain tensors (Figure 3) were determined by Ohashi's method[69] and graphically represented by the *Wintensor* software.[70] The principal strain eigenvalues (Table 2) were calculated using the *Win_Strain* software.[71]

GIXRD measurements of thin films. Grazing Incidence X-Ray Diffraction (GIXRD) measurements were performed at the XRD1 beamline of the ELETTRA synchrotron facility (Trieste, Italy) by using a wavelength of 1.00 Å and an incident angle of 0.1°. A 2D Pilatus was placed normal to the incident beam direction at 350 mm from the sample. Reciprocal space maps and their non-linear transformations were calculated from the measured data using the GIDVis software.[72]

Contact angle and stability measurements. Contact angle measurements were performed on (pXDA)$PbBr_4$ and (pXDA)Pb_2I_6 perovskite thin films. A droplet of water (50 μL) was added on the thin film surface and an image was captured with auEye UI-1240-SE–M (monochrome) camera (IDS Imaging Development Systems GmbH) controlled by LabVIEW (version 20).[73] The sample was illuminated from behind by a white LED, focused on the sample through a standard 100 mm lens. The amount of light on the sample was controlled by an adjustable iris diaphragm placed between the LED and the 100 mm focusing lens. A standard 16 mm manual focus lens with adjustable aperture mounted on a 5 mm extension was used to form the image of the drop on the sensor. Contact angles (CA) were calculated using the ImageJ software.[74] To test its environmental stability, the thin film of (pXDA)$PbBr_4$ was exposed to ambient conditions (air, light, temperature, humidity) and its XRD pattern was measured (every month) over a total period of six months.

SEM measurements. The perovskite films were deposited on aluminum SEM specimen stubs of 12.0 mm diameter, covered with carbon based electrically conductive double-sided adhesive discs. The samples were sputter coated with Cu (99.9% purity), using a Cressington 108 Auto sputter coater. Three cycles were performed at 30 mA and for 20 sec/cycle. Scanning electron microscopy (SEM) measurements were performed using an electronic microscope from FEI/Philips (model XL30 ESEM) in the high vacuum mode at a 20 kV acceleration potential using a secondary electron detector (SE).

Acknowledgements

The authors thank the Italian Ministry of Research for partial funding (Project PRIN 2017L8WW48, HY-TEC. Hybrid ThermoElectric Composites: Proof-of-concepts for low-T, n-type and flexible thermoelectrics) and the University of Insubria for postdoctoral funding granted to G.G.-E and K.F.K. We thank Dr. S. Milita for technical assistance in GIXRD measurements and data visualization.

Conflict of Interests

The authors declare no conflict of interest.

Data Availability Statement

The data that support the findings of this study are available from the corresponding author upon reasonable request.

Keywords: structure elucidation · lead halides · perovskites · powder diffraction · p-xylylenediamine

[1] J. Huang, Y. Yuan, Y. Shao, Y. Yan, *Nat. Rev. Mater.* **2017**, *2*, 17042.
[2] J.-P. Correa-Baena, A. Abate, M. Saliba, W. Tress, T. Jesper Jacobsson, M. Grätzel, A. Hagfeldt, *Energy Environ. Sci.* **2017**, *10*, 710–727.
[3] H.-S. Kim, I. Mora-Sero, V. Gonzalez-Pedro, F. Fabregat-Santiago, E. J. Juarez-Perez, N.-G. Park, J. Bisquert, *Nat. Commun.* **2013**, *4*, 2242.
[4] S. D. Stranks, G. E. Eperon, G. Grancini, C. Menelaou, M. J. P. Alcocer, T. Leijtens, L. M. Herz, A. Petrozza, H. J. Snaith, *Science* **2013**, *342*, 341–344.

[5] H. Chen, *Adv. Funct. Mater.* **2017**, *27*, 1605654.
[6] J. Li, Z. Han, Y. Gu, D. Yu, J. Liu, D. Hu, X. Xu, H. Zeng, *Adv. Funct. Mater.* **2021**, *31*, 2008684.
[7] M. A. Green, A. Ho-Baillie, H. J. Snaith, *Nat. Photonics* **2014**, *8*, 506–514.
[8] N. Arora, M. I. Dar, A. Hinderhofer, N. Pellet, F. Schreiber, S. M. Zakeeruddin, M. Grätzel, *Science* **2017**, *358*, 768–771.
[9] W. Zhang, X. Wu, J. Zhou, B. Han, X. Liu, Y. Zhang, H. Zhou, *ACS Energy Lett.* **2022**, *7*, 1842–1849.
[10] K. Lin, J. Xing, L. N. Quan, F. P. G. de Arquer, X. Gong, J. Lu, L. Xie, W. Zhao, D. Zhang, C. Yan, W. Li, X. Liu, Y. Lu, J. Kirman, E. H. Sargent, Q. Xiong, Z. Wei, *Nature* **2018**, *562*, 245–248.
[11] H. Tsai, W. Nie, J.-C. Blancon, C. C. Stoumpos, C. M. M. Soe, J. Yoo, J. Crochet, S. Tretiak, J. Even, A. Sadhanala, G. Azzellino, R. Brenes, P. M. Ajayan, V. Bulović, S. D. Stranks, R. H. Friend, M. G. Kanatzidis, A. D. Mohite, *Adv. Mater.* **2018**, *30*, 1704217.
[12] Y. He, L. Matei, H. J. Jung, K. M. McCall, M. Chen, C. C. Stoumpos, Z. Liu, J. A. Peters, D. Y. Chung, B. W. Wessels, M. R. Wasielewski, V. P. Dravid, A. Burger, M. G. Kanatzidis, *Nat. Commun.* **2018**, *9*, 1609.
[13] Z. Li, E. Hong, X. Zhang, M. Deng, X. Fang, *J. Phys. Chem. Lett.* **2022**, *13*, 1215–1225.
[14] M. Shellaiah, K. W. Sun, *Chemosensors* **2020**, *8*, 55, 10.3390/chemosensors80300.
[15] S. W. Eaton, M. Lai, N. A. Gibson, A. B. Wong, L. Dou, J. Ma, L.-W. Wang, S. R. Leone, P. Yang, *Proc. Natl. Acad. Sci. USA* **2016**, *113*, 1993–1998.
[16] R. K. Misra, B.-E. Cohen, L. Iagher, L. Etgar, *ChemSusChem* **2017**, *10*, 3712–3721.
[17] J. Almutlaq, W. J. Mir, L. Gutiérrez-Arzaluz, J. Yin, S. Vasylevskyi, P. Maity, J. Liu, R. Naphade, O. F. Mohammed, O. M. Bakr, *ACS Mater. Lett.* **2021**, *3*, 290–297.
[18] V. M. Goldschmidt, *Naturwissenschaften* **1926**, *14*, 477–485.
[19] L. Protesescu, S. Yakunin, S. Kumar, J. Bär, F. Bertolotti, N. Masciocchi, A. Guagliardi, M. Grotevent, I. Shorubalko, M. I. Bodnarchuk, C.-J. Shih, M. V. Kovalenko, *ACS Nano* **2017**, *11*, 3119–3134.
[20] W. Travis, E. N. K. Glover, H. Bronstein, D. O. Scanlon, R. G. Palgrave, *Chem. Sci.* **2016**, *7*, 4548–4556.
[21] Y. Fu, M. P. Hautzinger, Z. Luo, F. Wang, D. Pan, M. M. Aristov, I. A. Guzei, A. Pan, X. Zhu, S. Jin, *ACS Cent. Sci.* **2019**, *5*, 1377–1386.
[22] C. J. Bartel, C. Sutton, B. R. Goldsmith, R. Ouyang, C. B. Musgrave, L. M. Ghiringhelli, M. Scheffler, *Sci. Adv.* **2019**, *5*, eaav0693.
[23] L. Mao, C. C. Stoumpos, M. G. Kanatzidis, *J. Am. Chem. Soc.* **2019**, *141*, 1171–1190.
[24] K. Tanaka, T. Takahashi, T. Kondo, T. Umebayashi, K. Asai, K. Ema, *Phys. Rev. B* **2005**, *71*, 045312.
[25] I. B. Koutselas, L. Ducasse, G. C. Papavassiliou, *J. Phys.: Condensed Matter* **1996**, *8*, 1217.
[26] K. Zheng, T. Pullerits, *J. Phys. Chem. Lett.* **2019**, *10*, 5881–5885.
[27] Y. Chen, Y. Sun, J. Peng, W. Zhang, X. Su, K. Zheng, T. Pullerits, Z. Liang, *Adv. Energy Mater.* **2017**, *7*, 1700162.
[28] Y. Zhou, Y. Zhao, *Energy Environ. Sci.* **2019**, *12*, 1495–1511.
[29] Y. Yin, H. Cheng, W. Tian, M. Wang, Z. Yin, S. Jin, J. Bian, *ACS Appl. Nano Mater.* **2022**, *5*, 18879–18884.
[30] F. Ma, J. Li, W. Li, N. Lin, L. Wang, J. Qiao, *Chem. Sci.* **2017**, *8*, 800–805.
[31] H. Zhang, T. Yu, D. Li, A. Yang, X. Lai, C. Liang, Y. Lu, *ACS Appl. Energy Mater.* **2021**, *4*, 8774–8790.
[32] I. C. Smith, E. T. Hoke, D. Solis-Ibarra, M. D. McGehee, H. I. Karunadasa, *Angew. Chem. Int. Ed.* **2014**, *53*, 11232–11235.
[33] J. Hu, I. W. H. Oswald, S. J. Stuard, M. M. Nahid, N. Zhou, O. F. Williams, Z. Guo, L. Yan, H. Hu, Z. Chen, X. Xiao, Y. Lin, Z. Yang, J. Huang, A. M. Moran, H. Ade, J. R. Neilson, W. You, *Nat. Commun.* **2019**, *10*, 1276.
[34] K. Li, S. Yue, X. Li, N. Ahmad, Q. Cheng, B. Wang, X. Zhang, S. Li, Y. Li, G. Huang, H. Kang, T. Yue, S. U. Zafar, H. Zhou, L. Zhu, Y. Zhang, *Adv. Funct. Mater.* **2022**, *32*, 2200024.
[35] T. L. Leung, I. Ahmad, A. A. Syed, A. M. C. Ng, J. Popović, A. B. Djurišić, *Commun. Mater.* **2022**, *3*, 63.
[36] C. M. M. Soe, C. C. Stoumpos, M. Kepenekian, B. Traoré, H. Tsai, W. Nie, B. Wang, C. Katan, R. Seshadri, A. D. Mohite, J. Even, T. J. Marks, M. G. Kanatzidis, *J. Am. Chem. Soc.* **2017**, *139*, 16297–16309.
[37] Y. Chen, Y. Sun, J. Peng, J. Tang, K. Zheng, Z. Liang, *Adv. Mater.* **2018**, *30*, 1703487.
[38] H. Fu, *J. Mater. Chem. C* **2021**, *9*, 6378–6394.
[39] E. S. Vasileiadou, B. Wang, I. Spanopoulos, I. Hadar, A. Navrotsky, M. G. Kanatzidis, *J. Am. Chem. Soc.* **2021**, *143*, 2523–2536.
[40] B.-E. Cohen, Y. Li, Q. Meng, L. Etgar, *Nano Lett.* **2019**, *19*, 2588–2597.
[41] P. Atkins, J. De Paula, *Physical Chemistry for the Life Sciences*, Oxford University Press, **2006**, pp. 620–637.
[42] W. S. H. Ralph H. Petrucci, F. Geoffrey Herring, *General chemistry: principles and modern applications*, Prentice Hall, Upper Saddle River, NJ, **2002**, pp. 51–526.
[43] B. Saparov, D. B. Mitzi, *Chem. Rev.* **2016**, *116*, 4558–4596.
[44] L. Dou, *J. Mater. Chem. C* **2017**, *5*, 11165–11173.
[45] X. Zhang, G. Wu, W. Fu, M. Qin, W. Yang, J. Yan, Z. Zhang, X. Lu, H. Chen, *Adv. Energy Mater.* **2018**, *8*, 1702498.
[46] M. Safdari, P. H. Svensson, M. T. Hoang, I. Oh, L. Kloo, J. M. Gardner, *J. Mater. Chem. A* **2016**, *4*, 15638–15646.
[47] N. Marchal, E. Mosconi, G. García-Espejo, T. M. Almutairi, C. Quarti, D. Beljonne, F. De Angelis, *J. Phys. Chem. Lett.* **2021**, *12*, 2528–2535.
[48] A. Ummadisingu, A. Mishra, D. J. Kubicki, T. LaGrange, A. Dučinskas, M. Siczek, W. Bury, J. V. Milić, M. Grätzel, L. Emsley, *Small* **2022**, *18*, 2104287.
[49] R. Chiara, M. Morana, G. Folpini, A. Olivati, B. Albini, P. Galinetto, L. Chelazzi, S. Ciattini, E. Fantechi, S. A. Serapian, A. Petrozza, L. Malavasi, *J. Mater. Chem. C* **2022**, *10*, 12367–12376.
[50] S. Yuan, Z.-K. Wang, L.-X. Xiao, C.-F. Zhang, S.-Y. Yang, B.-B. Chen, H.-T. Ge, Q.-S. Tian, Y. Jin, L.-S. Liao, *Adv. Mater.* **2019**, *31*, 1904319.
[51] Y. Li, J. V. Milić, A. Ummadisingu, J.-Y. Seo, J.-H. Im, H.-S. Kim, Y. Liu, M. I. Dar, S. M. Zakeeruddin, P. Wang, A. Hagfeldt, M. Grätzel, *Nano Lett.* **2019**, *19*, 150–157.
[52] C. M. M. Soe, G. P. Nagabhushana, R. Shivaramaiah, H. Tsai, W. Nie, J.-C. Blancon, F. Melkonyan, D. H. Cao, B. Traoré, L. Pedesseau, M. Kepenekian, C. Katan, J. Even, T. J. Marks, A. Navrotsky, A. D. Mohite, C. C. Stoumpos, M. G. Kanatzidis, *Proc. Natl. Acad. Sci. USA* **2019**, *116*, 58–66.
[53] N. Li, Y. Yang, Z. Shi, Z. Lan, A. Arramel, P. Zhang, W.-J. Ong, J. Jiang, J. Lu, *iScience* **2022**, *25*, 103753.
[54] Q. Zhou, B. Liu, X. Shai, Y. Li, P. He, H. Yu, C. Chen, Z.-X. Xu, D. Wei, J. Chen, *Chem. Commun.* **2023**, *59*, 4128–4141.
[55] L. Jiang, J. Lu, S. R. Raga, J. Sun, X. Lin, W. Huang, F. Huang, U. Bach, Y.-B. Cheng, *Nano Energy* **2019**, *58*, 687–694.
[56] W. Song, T. Aernouts, *J. Phys.: Energy* **2020**, *2*, 021003.
[57] A. Dučinskas, G. Y. Kim, D. Moia, A. Senocrate, Y.-R. Wang, M. A. Hope, A. Mishra, D. J. Kubicki, M. Siczek, W. Bury, T. Schneeberger, L. Emsley, J. V. Milić, J. Maier, M. Grätzel, *ACS Energy Lett.* **2021**, *6*, 337–344.
[58] C.-Q. Jing, J. Wang, H.-F. Zhao, W.-X. Chu, Y. Yuan, Z. Wang, M.-F. Han, T. Xu, J.-Q. Zhao, X.-W. Lei, *Chem. Eur. J.* **2020**, *26*, 10307–10313.
[59] L. Dobrzycki, K. Woźniak, *CrystEngComm* **2008**, *10*, 577–589.
[60] C. Lermer, A. Senocrate, I. Moudrakovski, T. Seewald, A.-K. Hatz, P. Mayer, F. Pielnhofer, J. A. Jaser, L. Schmidt-Mende, J. Maier, B. V. Lotsch, *Chem. Mater.* **2018**, *30*, 6289–6297.
[61] D. H. Fabini, R. Seshadri, M. G. Kanatzidis, *MRS Bull.* **2020**, *45*, 467–477.
[62] E. I. Marchenko, V. V. Korolev, A. Mitrofanov, S. A. Fateev, E. A. Goodilin, A. B. Tarasov, *Chem. Mater.* **2021**, *33*, 1213–1217.
[63] T. Haeger, R. Heiderhoff, T. Riedl, *J. Mater. Chem. C* **2020**, *8*, 14289–14311.
[64] G. Uzurano, N. Kuwahara, T. Saito, A. Fujii, M. Ozaki, *ACS Mater. Lett.* **2022**, *4*, 378–384.
[65] M. E. Kamminga, G. A. de Wijs, R. W. A. Havenith, G. R. Blake, T. T. M. Palstra, *Inorg. Chem.* **2017**, *56*, 8408–8414.
[66] B. Febriansyah, D. Giovanni, S. Ramesh, T. M. Koh, Y. Li, T. C. Sum, N. Mathews, J. England, *J. Mater. Chem. C* **2020**, *8*, 889–893.
[67] A. A. Coelho, *J. Appl. Crystallogr.* **2003**, *36*, 86–95.
[68] TOPAS–R, V.3.0 (2005), Bruker AXS, Karlsruhe, Germany.
[69] Y. Ohashi in *Comparative crystal chemistry* (Eds.: R. Hazen, L. Finger), Wiley, NY, **1982**, pp. 92–102.
[70] W. Kaminski, 1.5 (2014) ed., http://www.wintensor.com (accessed April 18th, 2023).
[71] R. J. Angel, Win_*Strain Users Manual. A program to calculate strain tensors from unit-cell parameters*, http://www.rossangel.com, **2011**.
[72] B. Schrode, S. Pachmajer, M. Dohr, C. Röthel, J. Domke, T. Fritz, R. Resel, O. Werzer, *J. Appl. Crystallogr.* **2019**, *52*, 683–689.
[73] T. M. Rick Bitter, Matt Nawrocki, *LabVIEW: Advanced programming techniques*, CRC Press, Boca Raton, **2006**.
[74] C. A. Schneider, W. S. Rasband, K. W. Eliceiri, *Nat. Methods* **2012**, *9*, 671–675.

Manuscript received: May 15, 2023
Revised manuscript received: May 24, 2023
Accepted manuscript online: May 29, 2023